

1 **Diurnal to Seasonal Dynamics of Groundwater, Evaporation, and Hydrology**
2 **Fluctuations at the Bonneville Salt Flats Saline Pan**

3 **J. A. Bernau¹, B. B. Bowen^{1,2}, E. R. Pardyjak³, and E. L. Kipnis¹**

4 ¹Geology and Geophysics, University of Utah, Salt Lake City, UT, USA; ²Global Change and
5 Sustainability Center, University of Utah, Salt Lake City, UT, USA; ³Mechanical Engineering,
6 University of Utah, Salt Lake City, UT, USA

7 Corresponding author: Jeremiah Bernau (jeremiahbernau@gmail.com)

8
9 **Key Points:**

- 10 • Over four years of evaporation were estimated by using eddy-covariance measurements
11 to calibrate micrometeorological measurements.
- 12 • Saline pan albedo, which reflects water availability, can be used to calibrate evaporation
13 estimates.
- 14 • Seasonal to diurnal temperature fluctuations have significant impacts on groundwater
15 levels.
16

17 Abstract

18 Saline pans are environments with evaporite crusts, high-salinity surface and groundwater brines,
19 and low topographic gradients. These characteristics make them sensitive to diverse hydrological
20 processes. The Bonneville Salt Flats, a valued and changing saline pan, was investigated to
21 identify saline pan hydrology responses to diurnal to seasonal cycles. Seasonal changes in
22 evaporation and relationships between groundwater levels and environmental processes in saline
23 pans are not well understood. The results presented here, which improve characterizations of
24 saline pan water balances and movement, enable predictions of salt growth or dissolution
25 associated with geoengineering to mitigate the impacts of mining saline pans. Three months of
26 eddy-covariance evaporation measurements were collected, spanning a flooded to desiccated
27 surface transition. Two techniques, an artificial neural network and an albedo-based calibration
28 of the Penman equation, were evaluated and used to estimate evaporation with over four years of
29 inexpensive micrometeorological measurements. Albedo, a water availability proxy, inversely
30 correlated with evaporation. Shallow groundwater levels varied seasonally by >50 cm and daily
31 by >6 cm in response to temperature fluctuations. Groundwater level fluctuations should be
32 carefully interpreted as they may not reflect recharge or discharge. Evaporation had a minor, <10
33 cm y^{-1} , effect on groundwater levels. Surface moisture, primarily from rain, controlled
34 evaporation. Summer desiccated surface evaporation was $\sim 0.1 \text{ mm d}^{-1}$. The net annual water
35 balance was $< \pm 1.5 \text{ cm y}^{-1}$, indicating the saline pan stabilizes the water table. Surface dynamics
36 of these environmentally-sensitive and variable landscapes are increasingly important to
37 understand as water scarcity in arid environments rises.

38 Plain Language Summary

39 Saline pans are vast, awe-inspiring, salt-encrusted landscapes that form from the evaporation of
40 saline water. We describe four years of observations, including measured evaporation and
41 groundwater levels at the Bonneville Salt Flats saline pan. We examine how water moves
42 through this system over time. We tested inexpensive methods of estimating evaporation and
43 used these methods to study water balances. We found that the majority of water table changes
44 reflected temperature changes, not evaporation. Most evaporation at the saline pan center was of
45 rainwater. The salt crust acted as a barrier to evaporation of shallow groundwater. These
46 processes are important to understand as these environments are changed by increasing

47 desertification. The Bonneville Salt Flats saline pan formed when there was more regional water
48 and solute input into the saline pan and evaporation significantly exceeded precipitation; this
49 differs from current conditions. Additionally, seasonal fluctuations in groundwater levels in these
50 systems do not reflect regional changes in discharge and recharge.

51 **1. Introduction**

52 Saline pans are dynamic environments where hydrology, mineralogy, and landscape evolution
53 are strongly coupled (Rosen, 1994; Tyler et al., 2006). Evaporite-containing basins have become
54 increasingly important in the past century as desertification has increased and lithium and
55 potassium extraction and anthropogenic water use have led to the global decline of saline lakes
56 and pans. These changes can inadvertently increase sources of aerosolized dust and impact air
57 quality and human health (e.g. the Salton Sea and the Salar de Atacama) (Boutt et al., 2016;
58 Kipnis & Bowen, 2018; Marazuela et al., 2019b; Wurtsbaugh et al., 2017). Saline pan
59 environmental fluxes and surface properties change as they oscillate between flooding and
60 desiccation periods (Craft & Horel, 2019; Nield et al., 2015). The mechanisms that control
61 evaporation and hydrology within saline pans and how these processes change over time are not
62 fully understood. Environmental measurements can improve understanding of the mechanisms
63 and feedbacks between climate, hydrology, and the evolution of saline pans. This study uses a
64 suite of hydrological and meteorological measurements to observe feedbacks between the halite
65 crust, evaporation, and groundwater fluxes over four years at the Bonneville Salt Flats.

66 Hydrology is integral to understanding and interpreting saline pans (Rosen, 1994). These systems
67 form when saline minerals crystallize as surface water and groundwater evaporate. Groundwaters
68 in and around saline playas often represent regional flow paths' terminus (Lerback et al., 2019;
69 Rosen, 1994). Delineation of evaporation rates helps constrain long-term solute and hydrological
70 budgets and informs understanding of saline pan formation and alteration (Garcia et al., 2015;
71 Mason & Kipp, 1998). Improved knowledge of saline pan sediments and processes can inform
72 astrobiology, sedimentology, paleoclimatology, and evaporite-related resource management
73 (Lowenstein et al., 1989). Since saline pan waters can remain liquid across a wider range of
74 environmental conditions than fresh water environments and host and preserve microbial
75 ecosystems, saline pans are increasingly studied as Martian analogs (Benison & Bowen, 2006;
76 Benison & Karmanocky, 2014). Evaporite mineral formation and alteration rates are directly

77 influenced by hydrology and evaporation rates. Both regional micrometeorology and
78 understanding of climatic trends can be improved by studying and describing saline pans, which
79 can be very extensive ($>1000 \text{ km}^2$) (Craft & Horel, 2019; Kampf et al., 2005; Tyler et al., 2006).
80 Highly saline shallow or intermediate waters underlie approximately 16% of the earth's land area
81 (van Weert & van der Gun, 2012). Saline pan hydrology differs from other, more humid settings
82 in response to changes in evaporative demand, temperature, and regional recharge (Tyler et al.,
83 2006). Large diurnal water-level fluctuations have been observed in these systems (Turk, 1975).
84 High-salinity brines create gradients that can lead to density-driven groundwater convection
85 (Van Dam et al., 2009; Duffy & Al-Hassan, 1988; Fan et al., 1997; Wooding et al., 1997).
86 Differences in hydraulic conductivity and density between saline pans and regional groundwater
87 flow prevent groundwaters from mixing. Fresher regional groundwater flows along alluvial fans
88 and discharges at the surface around the edges of saline pans (DeMeo et al., 2003; Duffy & Al-
89 Hassan, 1988; Fan et al., 1997; Garcia et al., 2015; Huntington et al., 2014; Munk et al., 2021).
90 Although these landscapes are characterized by the remnants of evaporation (evaporites),
91 evaporation rates are minimal despite groundwater within cm of the surface (Kampf & Tyler,
92 2006). Low evaporation rates and numerical groundwater flow modeling of playas, including
93 saline pans, indicate that modern saline pans contribute to $<2\%$ of a basin's groundwater
94 discharge in the western United States (Jackson et al., 2018). This highlights saline pans' ability
95 to stabilize groundwater levels and associated landscape surfaces.

96 This work aims to use the Bonneville Salt Flats to investigate how saline pan hydrology,
97 specifically evaporation and groundwater levels, responds to processes occurring at daily to
98 seasonal time scales. Techniques to use long-term, inexpensive meteorological equipment
99 measurements to estimate saline pan evaporation rates are presented and evaluated. These results
100 and methods can help constrain environmental processes, coupling, and response rates to
101 environmental changes within other saline pans. This robust dataset is used to examine
102 mechanisms and controls upon saline pan water fluxes and water levels. Furthermore,
103 hydrological budgets can use these methods to improve understanding of the role and
104 mechanisms of groundwater evaporation upon evaporite development, resource evolution, and
105 landscape change.

106 2. Background

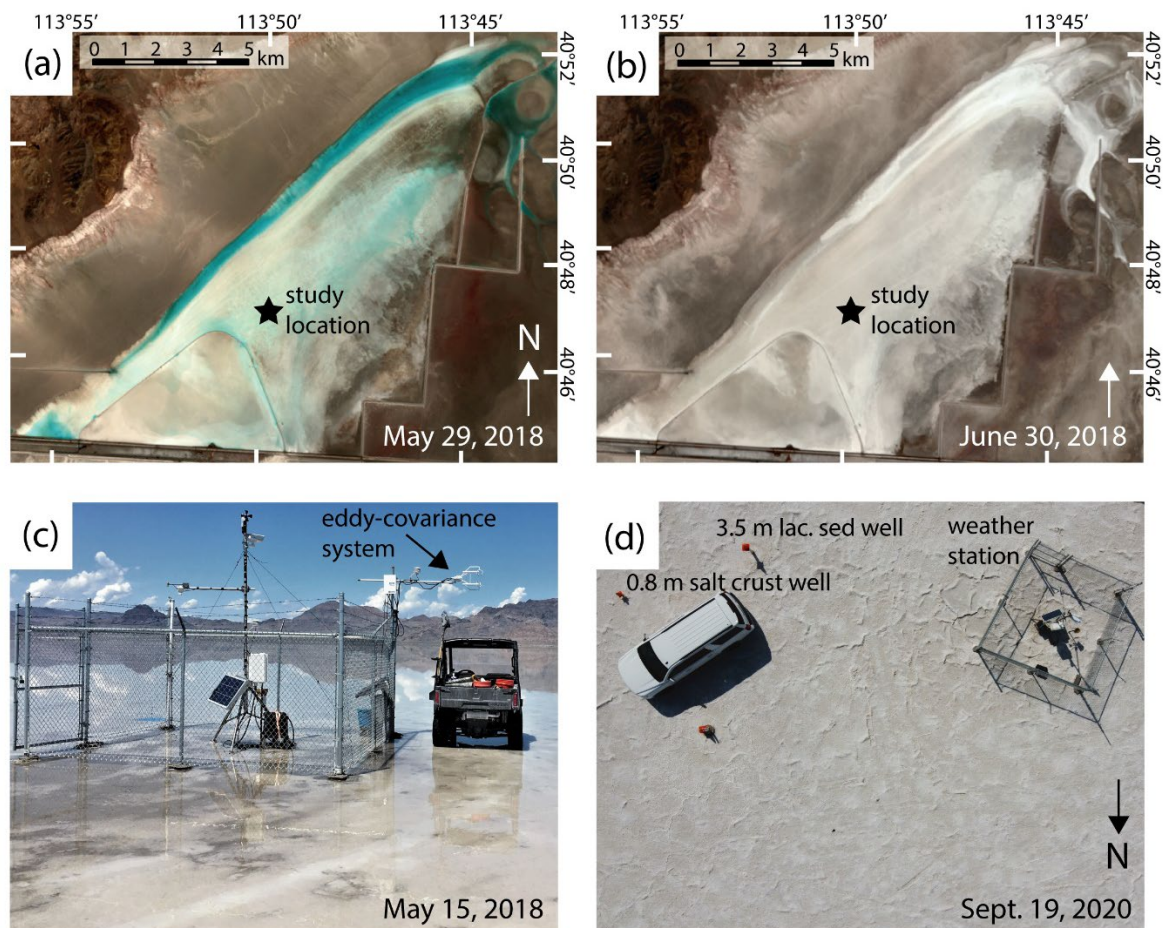
107 2.1. Hydrogeological setting

108 This study was conducted at the Bonneville Salt Flats (BSF), Utah, on traditionally
109 Newe/Western Shoshone and Goshute lands. BSF consists of a thin (<2 m) lens-shaped deposit
110 of halite and gypsum that overlays laminated carbonate lacustrine sediments (Bowen, Kipnis, et
111 al., 2018). Groundwater in this system is near or within 1 m of the surface and ranges from
112 hypersaline ($>1.2 \text{ g cm}^{-3}$) to saline ($1.10 \text{ to } \leq 1.19 \text{ g cm}^{-3}$) (Lines, 1979). The saline pan's
113 hydrology has been studied extensively since the 1960's (Kipnis & Bowen, 2018; Lines, 1979;
114 Mason & Kipp, 1998; Turk, 1973). BSF's largest hydrological fluxes are evaporation and
115 precipitation (Mason & Kipp, 1998). Surface water at BSF is sourced locally from rainfall and is
116 distributed across its surface by wind. Mason and Kipp (1998) reported that precipitation at the
117 edge of BSF was within 5% of precipitation at the saline pan's center, indicating that
118 precipitation is relatively consistent across the surface (Figure S1). BSF's water table's
119 potentiometric surface slopes away from the center of the saline pan, down to the northwest and
120 east, limiting lateral input of groundwater at the study location at the center of BSF (Lines, 1979;
121 Kipnis & Bowen, 2018). BSF is the drainage terminus at the northern end of a subbasin in Utah's
122 Great Salt Lake Desert. Since 1907, infrastructure south of BSF has limited water inputs from
123 the larger basin (Kipnis & Bowen, 2018).

124 Past BSF saline-pan evaporation estimates, from pan evaporation, the Bowen-ratio method, and
125 surface halite growth rates ranged from $1.3 \text{ to } 3 \text{ mm d}^{-1}$ when the surface was flooded to 0.001 to
126 0.50 mm d^{-1} when the surface is desiccated (Lines, 1979; Mason & Kipp, 1998). Tyler et al.
127 (1997) evaluated several evaporation techniques and found that only the eddy-covariance and
128 lysimeter techniques were sensitive enough to accurately measure saline pans' low evaporation
129 rates. Low evaporation rates from BSF's desiccated surface are comparable to other saline pans
130 and playas, which have average evaporation rates of 0.21 mm d^{-1} (Allison & Barnes, 1985;
131 Costelloe et al., 2011; DeMeo et al., 2003; Garcia et al., 2015; Hang et al., 2016; Jacobson &
132 Jankowski, 1989; Kampf et al., 2005; Lines, 1979; Malek & Bingham, 1990; Mardones, 1998;
133 Menking et al., 2000; Sanford & Wood, 2001; Schulz et al., 2015; Tyler et al., 1997; Ullman,
134 1985). Evaporation of groundwater from saline pans is so low that it is often within eddy

135 covariance measurement errors of 4 cm y^{-1} (0.1 mm d^{-1}), making it challenging to quantify
 136 groundwater evaporation from saline pans (Garcia et al., 2015; Kampf et al., 2005).

137 BSF's surface undergoes stages where it is flooded and desiccated. Annually, there are autumn
 138 and spring periods of surface flooding at BSF (Bowen et al., 2017). Surface moisture at BSF is
 139 directly related to albedo. Decreasing albedo correlates with increasing water availability (Craft
 140 & Horel, 2019). Surface flooding is uneven over the surface of BSF. A persistent seasonal pond
 141 occurs along BSF's northwest side. Past research and Landsat 8's normalized difference water
 142 index indicate that, after the western pond, this study's location at BSF's center, is the second-
 143 most moist area on BSF's crust (Figure 1) (Bowen et al., 2017; Craft & Horel, 2019).



145 **Figure 1.** Overview of study location. (a-b) Contrast-enhanced false-color Landsat 8 images (bands 5, 4, and 3 as
 146 red, green, and blue, respectively), showing the presence of water (blue) during representative (a) flooding and (b)
 147 desiccation period conditions (2018). The black star indicates the study location in the middle of BSF. The linear
 148 features to the east are brine drainage ditches. The parallel lines at the base are Interstate 80. (c) Flooded surface at
 149 the weather station site at the beginning of the calibration period looking to the southwest. (d) Image of the surface
 150 of the study location weather station and wells after a sustained dry period (vehicle for scale). Date is shown on the
 151 lower right corner of each image.

152 Anthropogenic processes alter BSF's hydrology. Up to several billion liters of groundwater are
153 harvested annually, leading to local decreases in groundwater level (Kipnis & Bowen, 2018;
154 Lines, 1979). Brine created by dissolving the evaporation mine's halite by-product with brackish
155 water from the alluvial fans of the mountains adjoining BSF to the west is introduced onto BSF
156 in February and March through an experimental geoengineering salt restoration program.
157 Cumulatively, more brine has been introduced into BSF than extracted through this program,
158 which started in 1998 (Figure S2).

159 2.2. Mineralogy and salinity impact hydrology

160 Saline crusts and water salinity substantially impact radiative, thermal, and evaporative fluxes.
161 Brines and evaporite crusts create osmotic resistance and physical impediments to groundwater
162 vapor fluxes, thereby severely limiting evaporation (Li & Shi, 2019; Nachshon et al., 2011, 2018;
163 Schulz et al., 2015). Water activity, the equivalent vapor pressure of the atmosphere in relation to
164 a brine, decreases with increasing brine salinity (Calder & Neal, 1984; Mor et al., 2018; Turk,
165 1970). Potential evaporation decreases with lowering water activities. BSF's predominantly
166 sodium-chloride brines have a water activity of ~ 0.74 (Text S2). A groundwater evaporation
167 extinction depth for saline pans was estimated at 0.5 m at Salar de Atacama (Marazuella et al.,
168 2019a).

169 Interpretation of groundwater levels requires an understanding of the factors that control water-
170 table levels. Tyler et al. (2006) showed that water table fluctuations in response to hydrological
171 forcings, such as precipitation and evaporation, are muted when the water-table depth is below
172 0.2 to 0.5 m. Temperature influences saline pans' water-table depths seasonally (Garcia et al.,
173 2015; Turk, 1973). On shorter timescales, diurnal temperature and air-pressure changes can also
174 influence the water-table levels by several cm and almost immediately impact water level (Turk,
175 1975). Temperature affects water level by altering the capillary surface tension and changing the
176 volume of air entrapped in pores (Meyer, 1960; Turk, 1975). The impacts of surface temperature
177 on water level decrease with increasing water depth.

178 3. Methods

179 The methods used in this study are discussed in more detail in Text S1, S2, and S3.

3.1. Eddy-covariance data

An EC 150 CO₂/H₂O open-path infrared gas analyzer (IRGA) and CSAT3 3-D sonic anemometer/thermometer open path eddy-covariance system (Campbell Scientific, Inc., Logan, UT) was installed at 2.6 m height along with an HMP45C temperature/relative humidity sensor (Vaisala, Vantaa, Finland). High-frequency IRGA and sonic data were collected at 20 Hz and slow-response temperature and humidity data at 1 Hz using a CR3000 (Campbell Scientific, Inc., Logan, UT). Data were collected near BSF's center from May to August 2018 (the calibration period, Figure 1C). Latent and sensible heat fluxes were calculated by applying the eddy-covariance technique with 30-minute averaging intervals. Standard turbulence-flux corrections and quality control measures were applied following Jensen *et al.* (2016). Data gaps in evaporation measurements determined during quality control were filled with values generated with an artificial neural network (Kang *et al.*, 2019). This study focuses on daily sums of evaporation, so ground heat flux was not measured. Sonic anemometer data were used to calculate BSF's aerodynamic roughness (de Bruin & Holstag, 1982; Nield *et al.*, 2013).

3.2. Weather-station data

Research-grade weather station data collected at 5-minute intervals spanned from September 27, 2016 to the Spring of 2021 (the study period). Incoming and outgoing longwave and shortwave radiation were measured with an Apogee SN-500 net radiometer (Logan, Utah, USA, installed June 6, 2017). Before June 2017, incoming and outgoing shortwave radiation were measured with LI-200R solar sensors pointing upwards and downwards (400 to 1100 nm; LI-COR, Lincoln, Nebraska). Additional sensors include a Vaisala PTB110 pressure gauge; Texas Instruments TR-525USW unheated tipping bucket rain gauge; Vaisala HMP60 air temperature and relative humidity sensor at 2 m; and a R. M. Young 05103 anemometer at 3 m. A Campbell Scientific soil temperature sensor buried at 10 cm depth and an Axis Communications web camera were also installed on June 6, 2017. Weather station data gaps were filled with regional environmental measurements, an artificial neural network, and linear extrapolation. Weather-station data averaged over 30-minute intervals was used to calculate albedo, potential evaporation adjusted for water activity (PE), and estimated evaporation using an artificial neural network (E_cANN) and an albedo-calibrated modification of the Penman-equation (E_cLow and E_cHigh).

210 Albedo (α) was calculated with Equation 1, where the sum of daily outgoing shortwave radiation
 211 (SW_{out}) between sunrise and sunset (dt) is divided by the sum of daily incoming shortwave
 212 radiation (SW_{in}) over the same period. Surface moisture was quantified with albedo
 213 measurements (Craft & Horel, 2019) and was confirmed using time-lapse imagery (Bernau &
 214 Bowen, 2020).

$$215 \quad \alpha = \frac{\int SW_{out} dt}{\int SW_{in} dt} \quad (1)$$

216 3.3. Potential evaporation

217 A modified Penman equation was used to calculate potential daily evaporation corrected for
 218 water activity (Equation 2) (Calder & Neal, 1984; Malek & Bingham, 1990). Transpiration at
 219 this site is negligible because it lacks macroflora.

$$220 \quad PE = \left(\frac{\Delta}{\Delta + \gamma} (R_n + H_g) + \frac{\gamma}{\Delta + \gamma} 15.36(0.75 + 0.0115U_2) \left(e_s - \frac{e}{\beta} \right) \right) 86400/\lambda \quad (2)$$

221 where PE is potential evaporation (mm d^{-1}); Δ is the slope of the saturation-vapor-pressure curve
 222 ($\text{kPa}/^\circ\text{C}$); γ is the psychrometric constant (kPa/K); β is the water activity (0.74); R_n is net radiation
 223 (W/m^2); U_2 is the wind speed at 2 m height (m/s); e_s is the saturation vapor pressure at
 224 temperature T (kPa); e is the vapor pressure (kPa); and λ is the latent heat of vaporization (J/kg)
 225 ($1 \text{ kg H}_2\text{O} = 1 \text{ mm H}_2\text{O}/\text{m}^2$). H_g is the ground heat flux, which could not be calculated with
 226 available equipment. Ground heat flux is negligible over daily timescales, and was not
 227 considered because only daily potential evaporation values were used to measure long term
 228 fluxes (Allen et al., 1998). Unless otherwise noted, PE in this work refers to PE corrected for
 229 water activity.

230 3.4. Estimated evaporation

231 Estimated evaporation (E_c) was calculated by multiplying PE by a crop coefficient (K_c)
 232 calibrated with the eddy-covariance data and a daily albedo value (Equation 3). The calibration
 233 was segmented for two albedo ranges: albedo <0.37 , and albedo ≥ 0.37 . Evaporation fell sharply
 234 and stabilized as the surface dried out, at an albedo of ≥ 0.37 . Two models were used to create
 235 evaporation estimates when the surface was desiccated to address variability between measured

236 and estimated evaporation (Figure S4). A dry surface K_c was multiplied by albedo in the first
237 model (E_{cHigh}). A constant scaling factor was used in the second model (E_{cLow}).

$$238 \quad E_e = K_c \frac{PE}{\alpha} \quad (3)$$

239 Implementing the methods of Kelley and Pardyjak (2019), artificial neural network models were
240 used to estimate evaporation (E_{cANN}). The input 30-minute average values of the weather-
241 station observations were trained to replicate evaporation measured by the eddy-covariance
242 method. The effectiveness different input parameters was assessed by comparing artificial neural
243 network model evaporation estimates to E_{cHigh} and E_{cLow} values (Figure S5). The model
244 discussed in this work incorporates humidity, air temperature, air pressure, wind speed,
245 shortwave radiation (net and in), longwave radiation (net and out), and time of day as inputs.
246 Because the model outputs were not normally distributed, the median value of each 30-minute
247 interval over 1000 models was used. The upper and lower quartile values are also shown to
248 demonstrate the variability in model output. Variability is considered a measure of model
249 robustness and generality (Kelley et al., 2020). Periods with larger interquartile ranges indicate
250 higher uncertainty in artificial neural network modeled evaporation values.

251 Eddy covariance equipment was only installed at BSF's center from May to August 2018,
252 making winter periods with low temperatures and high humidity outside of the artificial neural
253 network's training dataset. To test the effect of removing these conditions from the training
254 dataset, the artificial neural network was run with training data incrementally trimmed to remove
255 progressively lower humidity and higher temperature periods. Modeled outputs after each
256 increment were saved and then compared (Figure S5). When the training dataset was limited to
257 higher temperatures, winter evaporation estimates were elevated, indicating neural network
258 model outputs overestimate winter evaporation because they did not have cold winter
259 temperature in their training data. To counter this, neural network model outputs greater than
260 potential evaporation (PE) or two times greater than albedo-calibrated estimated evaporation
261 (E_{cHigh}) were replaced with the neural network's 25th percentile values. If the 25th percentile
262 values exceeded these parameters, model outputs were replaced with E_{cHigh} values.

3.5. Groundwater-level data

Pressure-temperature transducers (U20L-04 and U20L-01, Onset, Bourne, Massachusetts, USA) were installed in a 3.5-m deep well screened in lacustrine sediments (lacustrine sediment well) between December 2017 to June 2021. Pressure-temperature transducers were installed in a 0.8-m deep well screened within the salt crust (salt crust well) from September 2019 to September 2021. Both wells were within 20 m of the weather station (Figure 1D). Additional wells dispersed across the saline pan were also considered.

The water depth in the saline salt crust well was more representative of the water table. The 3.5-m deep well was less saline. To make the water levels in the 0.8 and 3.5-m deep wells more comparable their heads were corrected by using Equation 4 (Post et al., 2007) (Figure S6).

$$h_1 = \frac{\rho_2}{\rho_1} h_2 - \frac{\rho_2 - \rho_1}{\rho_1} z \quad (4)$$

where ρ_l is the reference density to adjust the sample to (the average annual density of halite-saturated brine, 1.21 g cm⁻³); ρ_l is the density of the well-water; h_2 is the height of the water level above a datum (sea-level) as was measured using a depth to water meter or pressure transducer; z is the elevation (above the sea-level datum) of the mid-point of the screened interval; and h_1 is the equivalent head relative to the datum.

Water levels in the 3.5-m lacustrine sediment wells changed in response to air pressure changes, indicating it did not have high barometric efficiency. Measured changes in water level were influenced by the differential between atmospheric pressure at the well and at the aquifer (McMillan et al., 2019). The median-of-ratio's and linear regression methods over hourly and daily timescales were used to determine well's barometric efficiency (Turnadge et al., 2019). Because the effect of air pressure changes upon water level was quantified, these changes could be removed from the observed water level changes to determine what water levels would be if the wells had a perfect barometric efficiency and their water levels did not change in response to air pressure changes (Figure S7). If applying the barometric efficiency to water levels increased their variability, the calculated barometric efficiency was not used and was assumed to be one.

Similar to barometric efficiency, daily and seasonal water level fluctuations were influenced by temperature; this effect is defined here as a well's thermal efficiency. The barometric efficiency

291 framework can be applied to calculating and applying corrections for thermal efficiency. Periods
292 with water movement in and out of the system or water levels above the surface are removed
293 from datasets before using them to determine a well's thermal efficiency with barometric-
294 efficiency-corrected water level measurements. Because of lags in temperature peaks with water
295 depth, daily ranges of water level and soil temperatures were used to calculate daily thermal
296 efficiencies with the median-of-ratios method. Weekly to monthly intervals were used to
297 calculate seasonal values of thermal efficiency with the median-of-ratio's method. The thermal
298 efficiency could be used to correct water levels to understand how they would change if
299 temperature fluctuations were not affecting levels.

300 The apparent specific yield was calculated with a water budget equation. The apparent specific
301 yield was determined from the change in water level over a period given a known change in
302 water balance (Gerla, 1992; Lv et al., 2021; Walton, 1970). The apparent specific yield was used
303 to quantify evaporation from groundwater changes in groundwater levels corrected for
304 barometric and thermal efficiency, and density.

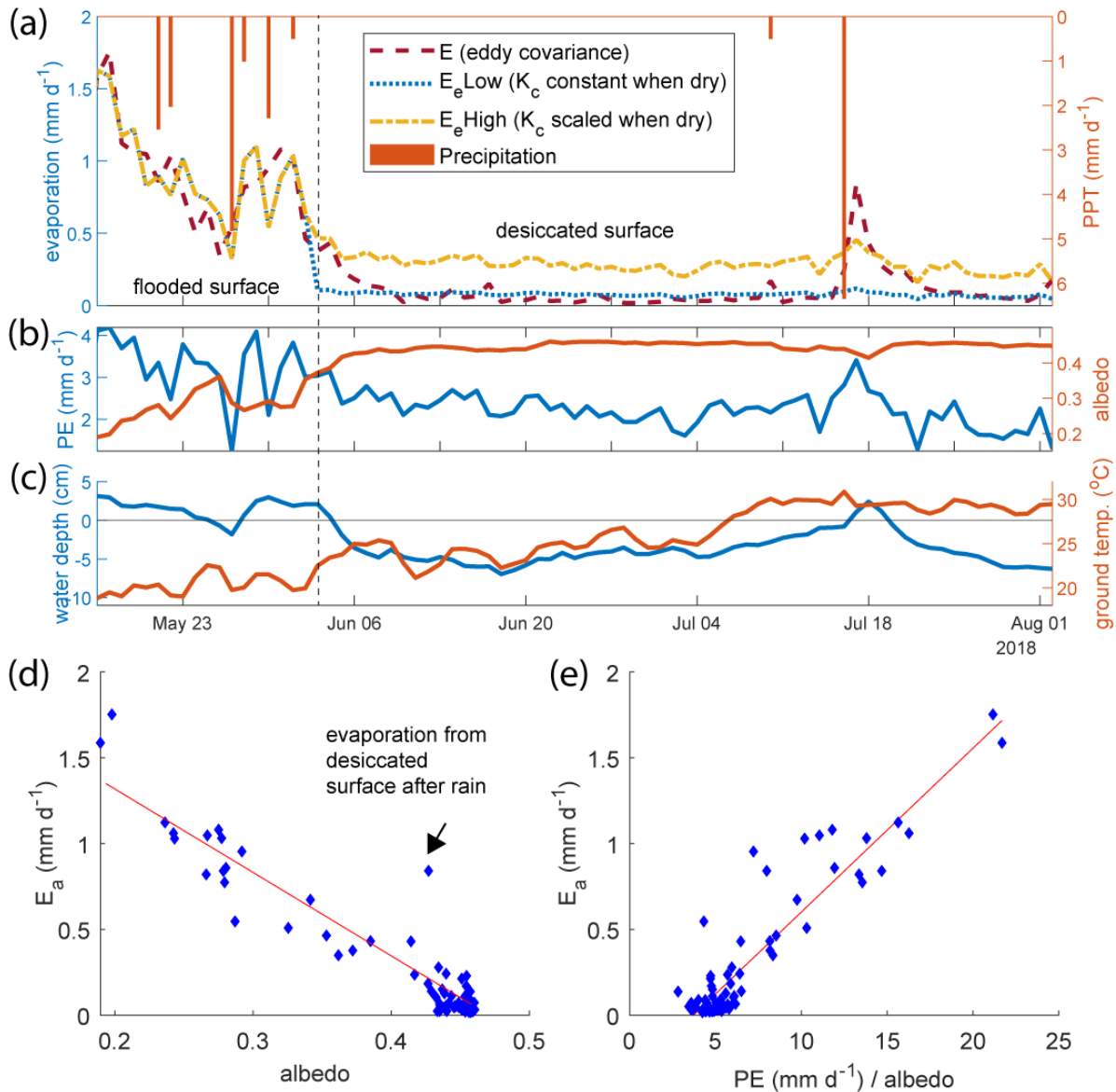
305 **4. Results**

306 The results of evaporation estimation methods applied during the calibration period are
307 reviewed, then the results of the full study period are described. Controls upon water level
308 fluctuations are described. Finally, daily fluxes in evaporation and water level throughout the
309 year are reported.

310 4.1. Calibration period

311 Evaporation rates from the surface were relatively high at the beginning of the calibration period,
312 when the surface was flooded (Figure 1C). Evaporation sharply decreased over time, briefly
313 increasing after rainfall (Figure 2A). Depth to groundwater reflected evaporation. Evaporation
314 was elevated when the water level was at or within 5 cm of the surface (Figure 2A and 2C).
315 During the desiccation stage, the average daily evaporation rate was $\sim 0.1 \text{ mm d}^{-1}$. The potential
316 evaporation rate, 2.3 mm d^{-1} , was >20 times higher than actual evaporation. The aerodynamic
317 roughness length was similar to other playas at $5.4 \times 10^{-4} \text{ m}$ (Jensen et al., 2016; Marticorena et
318 al., 2006). Evaporation was negatively correlated with albedo (Figure 2D, $r^2: 0.90$). Evaporation
319 was positively related to potential evaporation divided by albedo (Figure 2E, $r^2: 0.85$). This

320 relationship was used to create the albedo-calibrated estimated evaporation models (E_{cHigh} and
 321 E_{cLow}).



323 **Figure 2.** Environmental measurements and data relationships during the summer 2018 calibration period when the
 324 eddy-covariance system was at the Bonneville Salt Flats. (a) to (c) have the same x-axis values (a) Evaporation and
 325 precipitation (PPT). Eddy covariance evaporation was used to calibrate the albedo-adjusted evaporation estimates
 326 (E_{cHigh} and E_{cLow}). These two estimates provide bounds for evaporation during the desiccation stage. Evaporation
 327 from the artificial neural network is not shown during this period because it nearly matches evaporation values. (b)
 328 Potential evaporation (PE) is much higher than evaporation but does reflect its changes. Albedo gradually rises when
 329 the surface is flooded and plateaus during the desiccation stage. (c) Water level (adjusted for density and corrected
 330 for barometric efficiency), from 3.5 m deep well screened in lacustrine sediment, reflects changes in surface
 331 moisture indicated by albedo. Temperature is shown to highlight its impact on water levels. (d) The correlation
 332 between albedo and evaporation is robust. Evaporation after small summer rain events where the albedo does not
 333 decrease by much (July 17) is the exception to this relationship. (e) Linear correlation between evaporation and
 334 potential evaporation (PE) divided by albedo. This relationship was used to calibrate estimated evaporation (E_c)
 335 values in (a).

336 During the desiccation period, the relationship between evaporation and potential evaporation
337 divided by albedo was poor (r^2 : 0.05) so the two albedo-calibrated models were used to create
338 bounds for upper (E_{cHigh}) and lower (E_{cLow}) evaporation estimates (Figure 2A). These models
339 are dependent upon albedo, which is primarily controlled by surface moisture. However, surface
340 buckles and dust accumulation can also decrease local albedo, artificially increasing the apparent
341 surface moisture (Figure 1D).

342 Albedo stabilized during the desiccation stage, except after a 6.9 mm rain event in July 2018,
343 which led to a minor dip in albedo and a spike in evaporation. The dip in albedo was too minor
344 to impact the value of E_{cHigh} significantly, but the generally elevated evaporation levels of
345 E_{cHigh} compensate for this over periods greater than two weeks. This is reflected in the
346 cumulative values of measured evaporation, E_{cLow} , and E_{cHigh} during the calibration period.
347 E_{cLow} is below measured evaporation, while E_{cHigh} is above measured evaporation (Figure
348 S4C). Cumulative differences between the E_{cHigh} and E_{cLow} models encompass the uncertainty
349 of evaporation measurements during the desiccation period.

350 The measured daily evaporation values and the artificial neural network's estimated evaporation
351 values were effectively the same during the calibration period. During this period, cumulative
352 artificial neural network evaporation values were within 1% of the eddy-covariance evaporation
353 values (Figure S4).

354 4.2. Full study period

355 4.2.1. Evaporation estimation methods

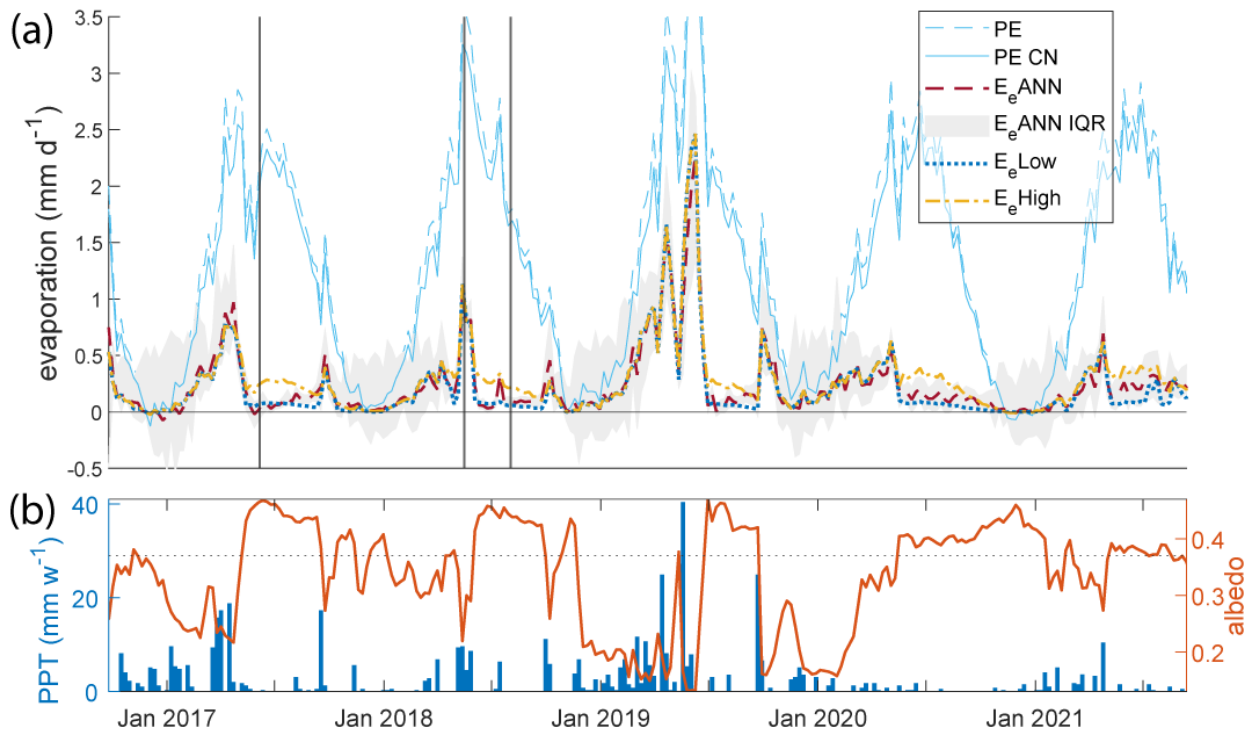
356 Over the full study period from Autumn 2016 to Autumn 2021 the artificial neural network's
357 estimated evaporation (E_{cANN}) values were similar to evaporation estimated by the calibrated
358 albedo-based models. In the summer months, E_{cANN} values were generally between the E_{cLow}
359 and E_{cHigh} values. E_{cLow} values were more similar to E_{cANN} values than E_{cHigh} values were,
360 except for periods immediately following rainfall. In contrast, the corrected artificial neural
361 network values had slightly higher evaporation estimates in winter than the other evaporation
362 estimation models. Furthermore, E_{cANN} values had large interquartile ranges during winter
363 months, indicating winter results were less robust because winter temperatures differed from the
364 calibration periods training dataset.

4.2.2. Evaporation over time

365
366 Evaporation was highest during the wet spring months and peaked after autumn flooding (Figure
367 3A). Evaporation was low in the summer when the salt crust was desiccated and low in the
368 winter when potential evaporation was minimal. There was a strong relationship between
369 evaporation and precipitation (Figure 3). Maximum potential evaporation peaked at $\sim 2.5\text{-}3.5$ mm
370 d^{-1} . The maximum model estimated evaporation rate was 2.5 mm d^{-1} . The length of spring
371 flooding varied between years, but the surface consistently desiccated by July. The autumn
372 flooding period was much smaller, and evaporation quickly decreased as the surface desiccated
373 or as potential evaporation fell. Autumn 2020 was unusually dry, and is the only time during the
374 study period to not have an autumn flooding period and an associated spike in evaporation.

375 Low albedo is generally associated with the higher estimated evaporation rates and results in
376 increased estimated evaporation values. Time-lapse imagery shows that increases in crust
377 roughness and dust accumulation depressed albedo. Rain dissolves surface halite and enables
378 dust to settle. As ponded water evaporates, new, highly reflective halite crystals form, leading to
379 high albedo values. Lower maximum albedo values during dry years (2020 and 2021), when a
380 lack of rain impairs this process, erroneously increase evaporation estimates (Figure 3B).

381 Figure 4 demonstrates that the cumulative precipitation and evaporation estimates are well-
382 aligned. The high evaporation model ($E_e\text{High}$), which overestimates evaporation, indicates
383 evaporation exceeds precipitation annually by ~ 2.0 cm y^{-1} on average. The $E_e\text{ANN}$ model
384 indicates precipitation exceeds evaporation by ~ 0.1 cm y^{-1} on average. Similarly, the $E_e\text{Low}$
385 model indicates precipitation exceeds evaporation by ~ 0.7 mm y^{-1} on average. The uncorrected
386 25th to 75th ANN models indicate evaporation exceeds precipitation by -0.5 to 5.0 cm y^{-1} . Water
387 balances vary annually. These differences are best seen with annual comparisons starting in
388 August, which is the last month of the year to be consistently desiccated. In 2018 and 2019, BSF
389 was water neutral to slightly water positive. All models show 2020 to have a negative water
390 balance, 2021 is similar to 2020. A negative water balance, indicating evaporation exceeds
391 precipitation, is typically limited to spring and summer months.



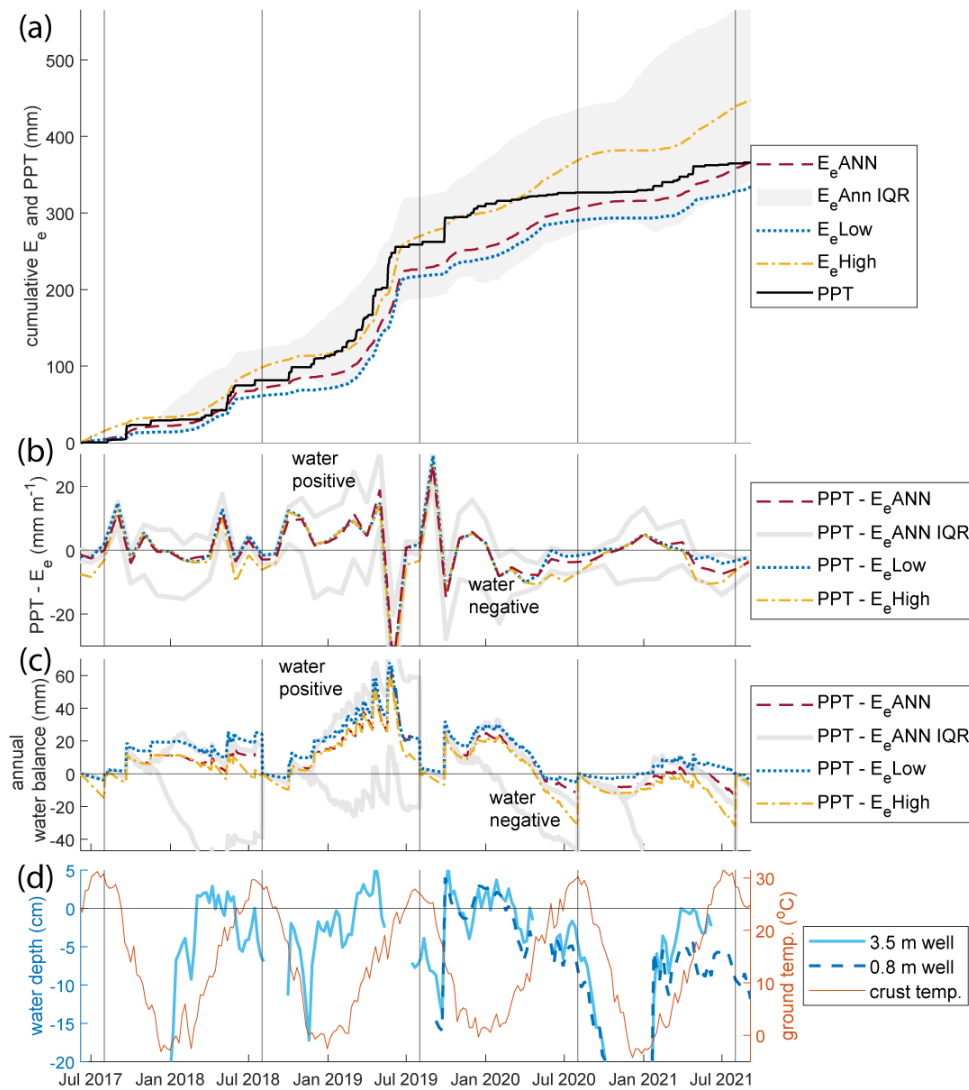
393 **Figure 3.** Weekly results of evaporation models applied to the entire dataset (Autumn 2016-Spring 2021) and
 394 associated environmental measurements. (a) and (b) have the same x-axis values. (a) Potential evaporation (PE and
 395 PE CN) far exceeded evaporation calculated with an artificial neural network and albedo-calibrated evaporation.
 396 Potential evaporation corrected for water activity (PE CN) was slightly lower (<20%) than the uncorrected potential
 397 evaporation (PE). The first vertical black line indicates when the Apogee SN-500 net radiometer and time-lapse
 398 camera were installed (June 6, 2017). Evaporation values before this period are not directly comparable to later
 399 evaporation values. The following two vertical black lines indicated the calibration period for this study (Figure 2).
 400 (b) Weekly precipitation and albedo measurements. The horizontal line indicates the cut-off value (0.37) for the
 401 albedo-calibrated evaporation models (E_e High and E_e Low).

402 4.2.3. Water balance from groundwater level

403 Temperature changes had a substantial impact on groundwater-level changes during dry periods.
 404 Significant decreases (<50 cm) in groundwater level occurred in dry autumns from the crust's
 405 cooling. Season thermal efficiency values were able to replicate these changes. These corrections
 406 showed that groundwater levels should have peaked in July, not May or June, indicating the
 407 effect of evaporation on summer water levels (Figure S2).

408 In general, groundwater evaporation rapidly decreases in the early summer as the groundwater
 409 levels declines. From May to August, ground temperatures increased $\sim 6^\circ\text{C}$, and groundwater
 410 levels in the 0.8 m deep well decrease by ~ 2 cm (~ 7 cm if corrected for temperature change). Of
 411 note, the average August groundwater depth in density-corrected wells at BSF's center is 10 cm
 412 (± 3 cm) (Figure S8), indicating that water levels stabilize in the subsurface after two to three

413 months of desiccation. This also makes this month ideal for year-to-year comparisons of water
 414 levels.



416 **Figure 4.** Measures of the water balance and water level from June 2017 to September 2021. All charts have the
 417 same x-axis values. Vertical black lines added at August 1 used to differentiate years because the water level
 418 stabilizes at roughly the same level in August each year, and the crust has been desiccated for at least one month
 419 prior to August. (a) Cumulative precipitation and estimated evaporation values. Evaporation increases after
 420 precipitation. These data indicate an annual mean net water balance (PPT - E_e) of 0.1 cm (E_eANN), 0.7 cm (E_eLow),
 421 -2.0 cm (E_eHigh). The E_eHigh model overestimates long-term evaporation. (b) Adapted Standardized Precipitation
 422 Evaporation Index (SPEI) where monthly evaporation is subtracted from monthly precipitation. Most months are
 423 water negative if potential evaporation is considered. Many water positive months were desiccated at the end of the
 424 month, e.g., November 2019, suggesting incorporation of precipitation into groundwater, overland flow of
 425 precipitation away from the system, or that evaporation was underestimated. (c) The cumulative net water balance
 426 (PPT - E_e) for each year (starting in August), 2018 and 2019 are water positive, 2020 and 2021 were water negative
 427 to water neutral for the E_eANN and E_eLow models. (d) Equivalent head water levels in the shallow salt crust (0.8 m
 428 deep) and lacustrine sediment (3.5 m deep) wells. The water level difference between the two wells shows that
 429 upward brine fluxes are buffering decreases in the saline pan water table in the summer. The water level in the wells
 430 begins to fall rapidly after August, when the air and ground temperatures decline.

431 The calculated apparent specific yield was 9% (standard deviation of 4%). This value likely
432 underestimates effective specific yield over longer drainage periods with deeper groundwater
433 levels, as the shallow crust is highly porous and permeable (average porosities of 23 to 29%).
434 Using specific yields of 5-13%, the average change in temperature-corrected water level
435 indicates that the normal groundwater evaporation rate from June to August is 0.06 to 0.15 mm
436 d^{-1} , these estimates would be halved if temperature impacts on groundwater were not considered.
437 If the majority of groundwater evaporation occurs from June to August, as inferred from changes
438 in groundwater levels, then 0.4 to 0.9 cm y^{-1} of groundwater evaporation is occurring annually.
439 This evaporation-rate estimate agrees with evaporation estimated with micrometeorological
440 techniques (0.1 mm d^{-1} during the desiccation stage, and net evaporation of -0.7 to 2 cm y^{-1}).

441 4.3. Diurnal fluxes: daily to seasonal changes

442 Evaporative fluxes are very low during the desiccation stage (Figure 5). Like other saline pans
443 (e.g. Kampf et al., 2005), it is challenging to identify diurnal patterns within evaporation
444 measurements from a desiccated saline pan. The half-hour median values of evaporation
445 measured with the eddy-covariance technique indicate higher evaporation occurs from sunrise to
446 noon. There are two evening spikes in evaporation, a short one at 18:00 MST and another at
447 23:00 MST. Evaporation is lowest in the morning before sunrise. In contrast, diurnal evaporative
448 fluxes during the flooding stage primarily reflected changes in potential evaporation.

449 Several other environmental parameters fluctuate daily during the summer desiccation stage
450 (Figure 5). Under the atmospheric tide (Chapman & Lindzen, 1970) air pressure generally rises
451 rapidly and peaks as evaporation with evaporation in the morning, it then falls until 20:00 MST
452 (sunset); and then rises and stabilizes in the evening. Albedo rises after 10:00 MST. Windspeed
453 is lowest at noon and highest in the evening, peaking at ~ 4 m/s at 21:00 MST.

454 The groundwater level in the salt crust well changes by ~ 6 cm from 09:00 to 18:00 MST each
455 day. During this period, air pressure changes by the equivalent of ~ 3 cm of halite-saturated brine
456 from 10:00 to 19:00 MST. Given this well's high barometric efficiency (>0.91), this change
457 would affect water levels by <0.5 cm. The ground temperature increased by 6 $^{\circ}\text{C}$ from its
458 minimum at 07:00 to its peak at 17:00 MST. Given this well's high summer diurnal thermal
459 efficiency (0.76), this change would affect water levels by 4.7 cm. The thermal efficiency

460 explains the majority of diurnal groundwater
 461 fluctuations, furthermore, the minimum and
 462 maximum water level points lag one hour
 463 behind these peaks in soil temperature, as
 464 would be suggested by a temporal lag for
 465 thermal diffusion, further support this
 466 hypothesis.

467

468

469

470

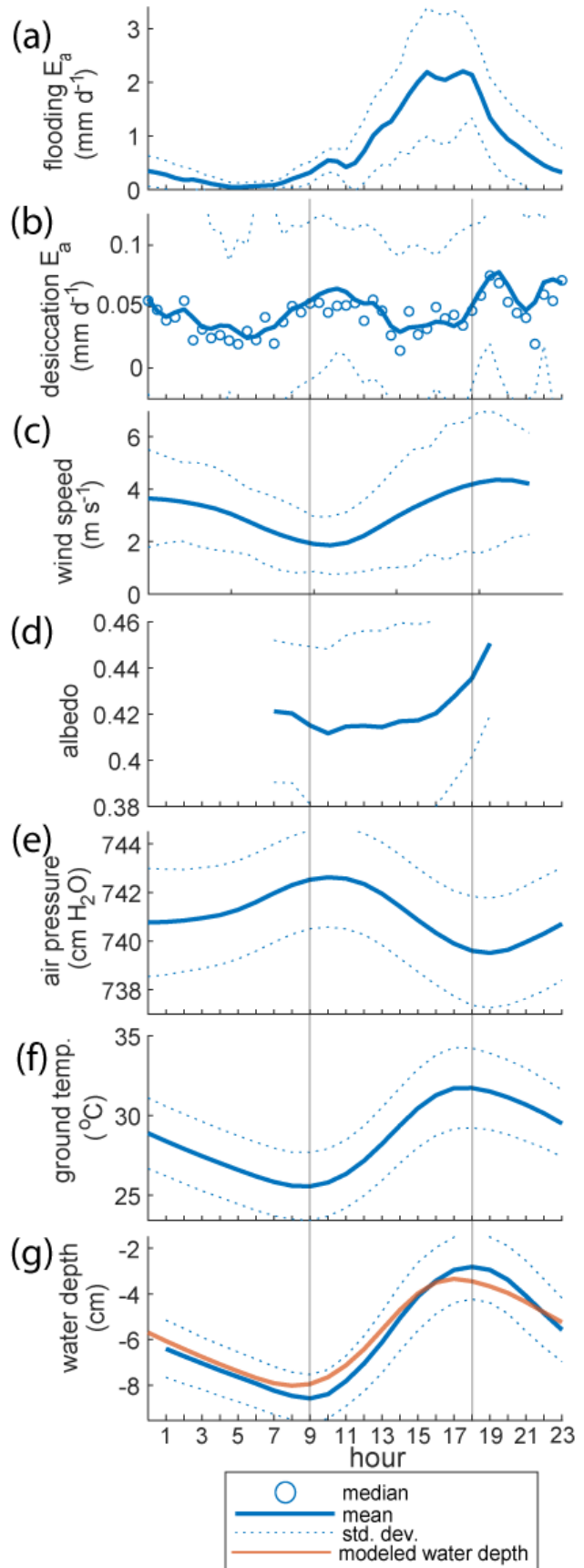
471

472

473

474 **Figure 5.** Diurnal fluxes over the salt crust. (a) Mean
 475 evaporation (smoothed fit) when the surface is flooded
 476 from the calibration period. (b to g) Mean fluxes when
 477 the surface is desiccated. Vertical gray lines added to
 478 highlight minimum and maximum water levels. (b)
 479 Median and mean evaporation (smoothed fit) from the
 480 desiccated surface during the calibration period. Note
 481 the peak in evaporation from the desiccated surface in
 482 the early morning (10 am) and the other peak in
 483 evaporation in the evening. (c) Wind speed is highest in
 484 the evening and lowest in the mid-morning. (d) Albedo
 485 is lowest in the early morning and rises throughout the
 486 day. (e) Air pressure (in cm of water with a density of
 487 1.2 g cm^{-3}). (f) Ground temperature at 10 cm depth.
 488 Mean water depth (from the 0.8 m salt crust well) is
 489 lowest during early morning and falls during the
 490 evening. The orange line shows the calculated water
 491 depth change due to the well's thermal efficiency,
 492 demonstrating the majority of diurnal water fluctuations
 493 are attributable to temperature fluctuations.

494



495 Seasonal trends in diurnal groundwater water-level fluctuations in the shallow salt crust well
496 indicate that the maximum range in groundwater levels reflects seasonal temperature change
497 (Figure 6). The well's highest diurnal thermal efficiencies occurred in summer months and daily
498 changes in water depth were most correlated with maximum soil temperature. Groundwater
499 levels increased sharply after rainfall and fell gradually in the subsequent weeks. Groundwater
500 level fluctuations are highest when the water table is 4 to 8 cm below the surface on average.
501 Diurnal temperature swings at the water table-vadose zone interface were muted by increasing
502 groundwater depth and the insulating property of the ground in autumn to winter. Similarly,
503 diurnal temperature variations were muted when the water table was at the surface (Figure 6B).

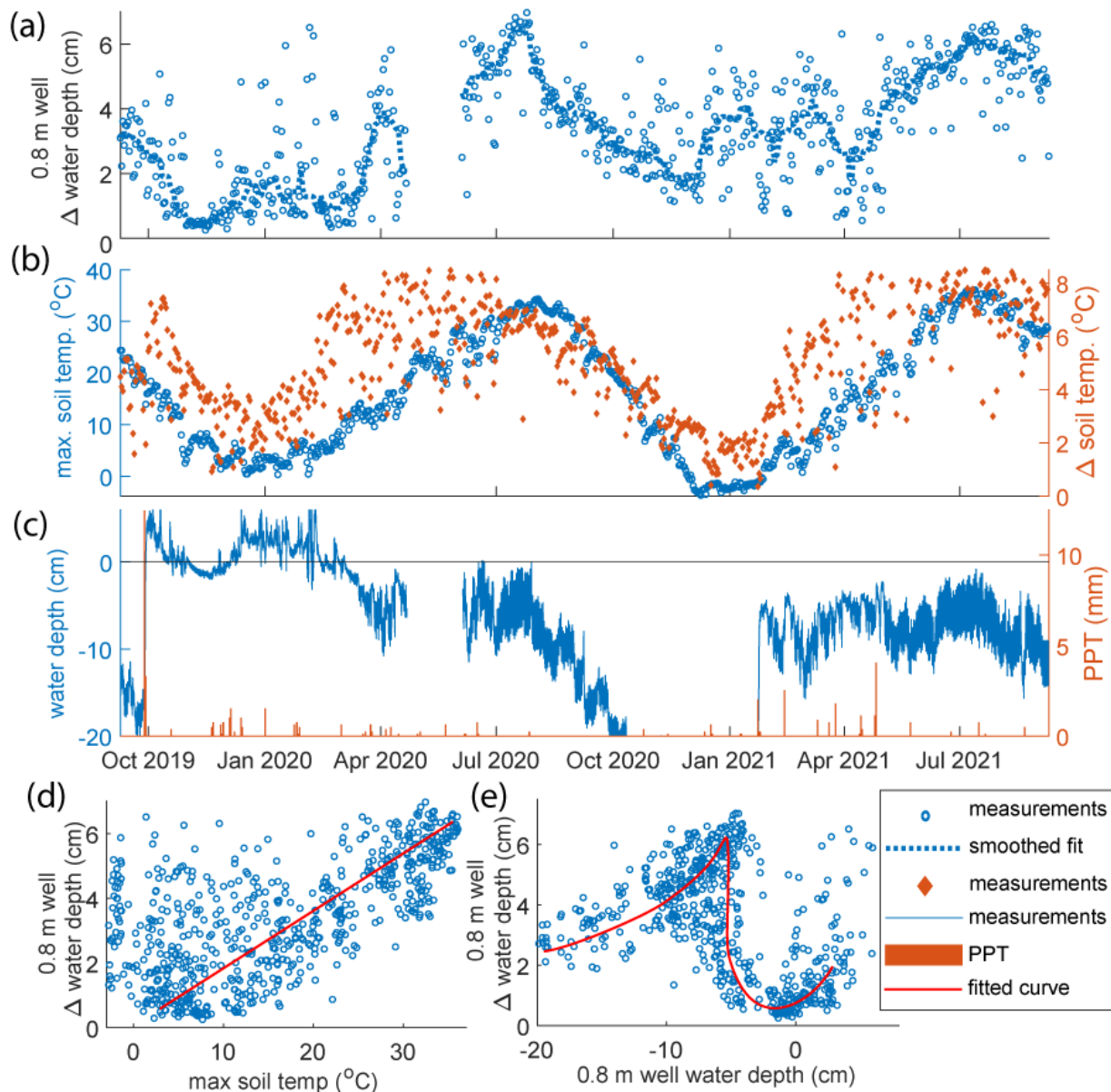
504 **5. Discussion**

505 The hydrological system at BSF is discussed here through the lens of groundwater levels, diurnal
506 fluctuations, seasonal changes in surface water, and overall water balances. These results'
507 implications are then discussed.

508 1.1. Daily to seasonal changes in groundwater level

509 Because evaporation rates for saline pans are so low and because their water levels can be so
510 variable throughout the year, the controls on water-table levels must be understood if
511 groundwater levels are used to interpret local to regional hydrological balances. Near-surface
512 ground temperature, followed by air temperature, when scaled using a seasonal or daily thermal
513 efficiency values predicted the majority of groundwater level fluctuations during periods with
514 little water movement in or out of the system.

515 Air pressure, which mirrors temperature changes, was previously shown to influence diurnal
516 groundwater-level fluctuations in saline pans (Macumber, 1991; Sieland, 2014; Turk, 1975).
517 However, given the high barometric efficiency of the 0.8-m salt crust well, air pressure appears
518 to play a minor (<10%) role in diurnal groundwater level fluctuations. Temperature changes,
519 which were previously shown to alter the surface tension in capillary pores and the volume of
520 pore-entrapped air (Meyer, 1960; Turk, 1975), are the primary control upon groundwater level
521 changes when the system is water neutral.



523 **Figure 6.** Daily water level changes in the 0.8 m salt crust well and associated daily environmental values.
 524 Smoothed fitted lines added to (a) to assist data interpretation. (a) Daily Δ water level ranges between \sim 0.5 to 7.0 cm
 525 throughout the year. Daily Δ water level are consistently high in the middle of the summer and are lower, with some
 526 days of high variation, in the autumn and winter. (b) Daily maximum 10-cm depth soil temperature and Δ soil
 527 temperature. (c) Daily precipitation and 30-minute intervals of measured water depth. Rainfall during this period
 528 was very low and contributed to a small minority of diurnal water level changes. (d) The daily Δ water depth in the
 529 0.8 m salt crust well correlates most strongly with maximum daily soil temperature. (e) The water table depth
 530 influences daily Δ water depth. Daily Δ water level is higher when the water level is between \sim 4 to 8 cm below the
 531 surface.

532 Predicted diurnal water-level changes were slightly lower than observed groundwater water-level
 533 changes, suggesting variability in diurnal thermal efficiency. Thermal efficiency models or
 534 applications of thermal efficiency to predict groundwater levels could be improved by
 535 incorporating additional inputs and numerical modeling. For example, water levels and lags from

536 thermal dispersion when water levels are lower could be incorporated. Seasonal and daily values
537 of thermal efficiency differ and were uncorrelated. There is no pattern between well parameters
538 and diurnal thermal efficiency values. Seasonal values of thermal efficiency, however, are
539 related salt crust thickness. Wells in areas with thicker evaporites (which are more porous) being
540 less affected by water level changes than wells in areas with little to no evaporites, which are
541 hosted in fine grained lacustrine sediments.

542 Previous studies indicate that the shallow water tables in playas can rise above the surface when
543 air pressure drops (Mason & Kipp, 1998; Turk, 1973; Tyler et al., 2006). Spontaneous water
544 level rise above the surface from only a reduction in air pressure was not observed during this
545 study. However, there were periods where the water table did change rapidly when the water
546 level was near the surface with little precipitation (<2 mm). For example, time-lapse imagery and
547 pressure transducer data in June 2021 show surface water following a minor rain event along
548 with rapid increases in groundwater levels (6 cm rise in 30 minutes), water in a small pond rose
549 to flood the crust surrounding it during this period. The water levels quickly returned to prior
550 levels in the hours following this event. These observations are consistent with the Lisse effect
551 (Heliotis & DeWitt, 1987). The Lisse effect occurs when rain traps air in the unsaturated zone, as
552 the air volume is changed by air pressure fluctuations or as it warms and expands it displaces
553 water, which can rise into wells, and in this case, breaks in the salt crust surface. Similar
554 observations in other saline pans may be explained by the Lisse effect.

555 Estimated evaporation values indicate that the halite crust severely limits evaporation of
556 groundwater. This research corroborates previous work that demonstrated negligible
557 groundwater evaporation from saline pans (Jackson et al., 2018; Kampf et al., 2005). The
558 consistent groundwater level in August at 9 cm (± 2 cm) below the surface across several years
559 indicates falling groundwater levels hinder evaporation.

560 Seasonal variation in groundwater levels make it challenging to interpret annual net water
561 balances from groundwater level changes. If only spring to summer months are considered,
562 groundwater evaporation would be 0.4 to 0.9 cm y^{-1} . This result is consistent with
563 micrometeorological evaporation estimates. Differences between annual water balance estimates
564 for the saline pan's center originate from uncertainties in estimating specific yield or

565 evaporation, lateral water movement, or the eddy-covariance technique's sensitivity, which was
566 near measurement error when the surface was desiccated.

567 The effect of temperature on groundwater levels should influence seasonal changes in
568 evaporation. If winter rain decreases the water-table depth, then later temperature increases will
569 increase groundwater levels, increasing groundwater availability for evaporation. This effect
570 would increase spring evaporation; however, it would likely be small given annual estimated
571 water balances ($<1 \text{ cm y}^{-1}$ evaporation increase). Bernau and Bowen (2021) previously described
572 apparent vertical brine fluxes from differences between the 0.8 and 3.5-m well equivalent head
573 measurements. An apparent upward gradient occurred in the summer, and a downward flux
574 occurred in the winter. Vertical gradients originate from differences in temperature effects upon
575 water level between salt crust and the underlying lacustrine sediment aquifer. The deeper
576 lacustrine sediment aquifer differs from the overlying evaporite-hosted aquifer because it is
577 shielded from temperature fluctuations, is thicker, and has much smaller pores.

578 At BSF's center, vertical fluxes and incorporation of rainwater into the lacustrine aquifer appears
579 to be minor. The mean groundwater transit time measured with carbon-14 from the 3.5-m
580 lacustrine sediment well was 10-15 thousand years old (Lerback et al., 2019). However, the same
581 study identified modern tritium in samples, indicating some vertical mixing and integration of
582 rainwater. In general, rainwater integration into the subsurface at BSF's center appears to be
583 limited. This interpretation is supported by most tritium measurements that were made on BSF
584 groundwater samples collected from 1992 to 1993, where wells at the center of BSF, with
585 consistently high water levels, had lower tritium concentrations than wells at the edge of BSF
586 (Mason et al., 1995).

587 5.2. Diurnal changes in evaporation

588 Diurnal evaporation fluctuations during the desiccation stage reflect changing evaporative
589 potential and water availability (Figure 6). The subtle morning increase in evaporation, which
590 has been documented in other saline pans (Malek & Bingham, 1990; Sanford & Wood, 2001),
591 was interpreted as the evaporation of groundwater from the overnight rehydration of the salt
592 crust (Malek & Bingham, 1990). The 18:00 MST peak in evaporation is associated with the
593 diurnal peak in groundwater level and temperature. This evaporation peak suggests that some of

594 the groundwater from daily water-level fluctuations increases near-surface water availability.
595 The 23:00 MST peak in evaporation is associated with the day's highest windspeed.

596 5.3. The flooding-evaporation-desiccation cycle

597 Saline pan sediments are interpreted through the flooding-evapoconcentration-desiccation cycle.
598 This cycle is enhanced through evaporative and hydrological observations (Bowen et al., 2017;
599 Lowenstein & Hardie, 1985). The desiccation stage describes periods when the surface is dry and
600 albedo is high. Bowen *et al.* (2017) used the Standardized Precipitation Evaporation Index
601 $[(\text{precipitation} - \text{evaporation})/\text{variance}]$ to calculate if the surface was in the flooding,
602 evapoconcentration, or desiccation stage. When this index uses potential evaporation, it reflects
603 seasonal trends in flooding and desiccation. However, when estimated evaporation is used in this
604 index, many more months have a positive water balance, suggesting longer flooding periods or
605 uptake of precipitation into the subsurface (Figure 4B and C). An alternative method to interpret
606 these stages is with albedo. Rapidly declining albedo indicates flooding, increasing albedo
607 indicates evapoconcentration, and a constant elevated albedo indicates the desiccation stage.

608 5.4. Saline pan water balance

609 There are three endmembers for the natural water budget at BSF: (1) the system is water neutral,
610 with evaporation equaling precipitation, (2) rainfall exceeds evaporation, and (3) evaporation
611 exceeds precipitation.

612 5.4.1. Water addition

613 Precipitation is the primary water input BSF. If anthropogenic brine, introduced as part of a
614 mining mitigation project, is ~10-80% of the annual water contributed to the southwestern part
615 of BSF (distributed over 20-50 km², Figure S2). Water inputs from snow or surface condensation
616 such as dew, which would further decrease the calculated volume of groundwater evaporation,
617 were assumed to be negligible in this study. If introduced brine and precipitation were evenly
618 distributed over a 120 km² area, precipitation is 90 to 100% of BSF's annual recharge, with the
619 remaining water being anthropogenically introduced. Past studies indicated other inputs such as
620 vertical water fluxes, overland flow, or lateral groundwater movement are <1% of the incoming
621 water budget at BSF (Lines, 1979; Mason & Kipp, 1998).

622 The distribution of surface water at BSF is uneven. Water accumulates in the low-lying
623 ephemeral western pond. When the surface is flooded, precipitation can flow downhill to this
624 pond. The seasonal pond increases evaporation at the weather station study site only when it
625 extends to the weather station or when wind redistributes surface water over the playa (Bowen et
626 al., 2017; Craft & Horel, 2019). Contributions to the pond from anthropogenic brine appear to
627 have had a negligible impact on measured evaporation at the study location. If anthropogenic
628 brine were significant at the study location, evaporation would exceed precipitation when the
629 surface was wet, which was not observed. If evaporation from the western pond were included in
630 estimating BSF's annual water budget, the ratio of evaporation to precipitation would increase.
631 Lateral subsurface flow at the study location is considered negligible because of the site's low
632 topography and groundwater's potentiometric surface is a local high near the study location.

633 5.4.2. Water removal

634 Water is currently removed from the saline pan by evaporation, groundwater extraction for
635 potash production, and surface and subsurface flow away from the site (Mason & Kipp, 1998).
636 Overland flow redistributes and concentrates water at the western part of BSF. However, this
637 only occurs when the water level is near the surface. Removal of surface or groundwater would
638 increase the local ratio of precipitation to evaporation (which is suggested by the E_c Low
639 evaporation model).

640 Evaporation was previously estimated to contribute to 80% of BSF's annual discharge (Mason &
641 Kipp, 1998). Uncertainties with the evaporation calculation are whether albedo and evaporation
642 continue to scale consistently in the winter and if the consistency of the year-to-year albedo
643 value relative to surface moisture. This relationship between albedo surface moisture is most
644 important when the surface is wet and evaporation is high. Kampf *et al.* (2005) found that albedo
645 can be lower in the more arid, dry parts of a saline crust, demonstrating that the relationship
646 between albedo and evaporation deteriorates under extended aridity. Cumulative evaporation
647 estimated with the artificial neural network was within 5% of the cumulative rainfall. These
648 values show that most of the study site's water budget is contributable to evaporation and
649 precipitation. The net annual water budget at BSF's center during this study was $0.5 \pm 1.5 \text{ cm y}^{-1}$
650 (Figure 4A). Evaporation from the desiccated surface was 3-10 times lower than that previously

651 estimated by Mason and Kipp (1998) using Bowen-ratio energy balance systems. Mason and
652 Kipp corrected for this in their calibrated model of BSF's water budget, with precipitation
653 exceeding evaporation by 15%, which aligns best with E_{cLow} evaporation model (precipitation
654 is 10% greater than evaporation).

655 5.4.3. Anthropogenic impacts upon the water balance

656 Anthropogenic water removal for potash production is two to three times less than anthropogenic
657 water introduced for mining mitigation (3-5% of annual discharge). However, added water is
658 more available for evaporation, dampening its offset on the total groundwater volume.
659 Furthermore, brine is removed from and introduced to different parts of BSF. Groundwater is
660 extracted year-round, while brine is only introduced in the winter. Removal of groundwater for
661 potassium production lowered well water levels near the extraction ditches, this signal is most
662 evident in thermal-efficiency-corrected groundwater levels (Figure S2).

663 The impact of brine extraction on groundwater levels at BSF's center is indiscernible. The
664 monthly average water level at BSF's center is consistent between March to September from
665 year to year, regardless of the volume of monthly groundwater extraction during the study
666 period. Decreases to groundwater levels by would increase uptake of precipitation into the
667 ground, creating water balances where precipitation exceeds evaporation, which was indicated
668 by E_{cLow} evaporation and BSF's calibrated mass balance model (Mason & Kipp, 1998).

669 5.5. Implications for evaporite growth and dissolution

670 These and prior observations of saline-pan evaporation rates and surface features indicate that
671 once a salt crust has formed and desiccated, evaporite growth is slow to negligible (Bernau &
672 Bowen, 2021; Kampf et al., 2005). Groundwater evaporation is minimal once a crust has
673 desiccated, indicating that salt crusts stabilize and preserve groundwater levels, indirectly
674 stabilizing the surface. Without saline crusts, playas become ablation surfaces, creating
675 significant dust sources (Rosen, 1994).

676 There must be a significant upward gradient for groundwater flow or lateral water input for
677 saline pans to form primarily from groundwater. Currently BSF does not receive such fluxes

678 (Kipnis & Bowen, 2018; Mason & Kipp, 1998). As Rosen suggested (1994), preservation of
679 evaporite systems is unlikely unless they are actively fed from external water sources and are in
680 tectonic settings that support their accumulation and preservation. Alternatively, under little
681 water input, these systems form very slowly or become deflation surfaces. Kampf *et al.* (2005)
682 determined that preserved subaerially-formed efflorescent crusts at Salar de Atacama could have
683 formed from a desiccated saline pan surface at net evaporation rates of 2 mm y^{-1} .

684 The sediments in saline pans suggest that most evaporite deposition occurs under conditions
685 when there is enough surface moisture available for evaporation and evaporation exceeds
686 precipitation. This moisture also decreases the surface albedo, increasing the absorption of solar
687 energy (Lowenstein & Hardie, 1985). Under wetter conditions in the past, overland flow into
688 BSF from the surrounding area would have contributed additional solutes to BSF by dissolving
689 and transporting efflorescent crusts. By directly and indirectly reducing groundwater levels and
690 water availability for evaporation (Marazuela *et al.*, 2020), anthropogenic activities alter the
691 balance between water input and evaporation within saline pans, leading growing saline pans to
692 stabilize and stable saline pans to decline over time. Similarly, global warming may also
693 influence some saline pans by reducing water inputs into saline pans and increasing halite
694 solubility through groundwater warming. Therefore, changes saline pans extent over time are
695 indicators of regional trends and changes in groundwater availability.

696 **6. Conclusions**

697 Evaporation estimates made with an ensemble of methods demonstrate that the center of the
698 Bonneville Salt Flats saline pan is water neutral to slightly water positive. Precipitation equals
699 or exceeds evaporation at the center of this saline pan. Limited evaporation stabilized the local
700 water table, periods with positive water balances contributed to the crust's gradual dissolution
701 over the past century. Sedimentologically, the current neutral water balance indicates the
702 limited capability of groundwater evaporation to contribute to evaporite deposition in modern
703 and ancient saline pans.

704 The methods utilized and evaluated in this work demonstrate that saline pan evaporative fluxes
705 can be estimated with inexpensive micro-meteorological equipment or groundwater level
706 monitors, but that calibration of these approaches with robust eddy flux station measurements

707 is needed. Understanding saline pan processes, such as the inverse correlation between surface
708 moisture and albedo and the positive correlation between ground temperature changes and
709 groundwater level, is critical to utilizing these methodologies and interpreting saline pans.

710 Saline pan landscapes are dynamic and rapidly evolve in response to climate change and
711 changes in water and mineral balances. Water extraction alters the water balance. Lowered
712 groundwater levels lead to a decrease to cessation in surface evaporite growth. Evaporite crust
713 loss can increase dust production potential. Long-term multi-parameter monitoring of these
714 systems would allow us to gain new insights and understand how these systems will change in
715 response to environmental stressors and how these changes will affect water supplies to dust
716 sources. Furthering our understanding of saline pans' dynamism will enable us to effectively
717 interpret and use these dynamic landscapes as sensitive indicators of regional hydrological
718 fluctuations.

719 **Acknowledgments**

720 We thank Ross Petersen, Nipun Gunawardena, Alex Bingham, Alexei Perelet, Jory Lerback,
721 Elliot Jagniecki, Boe Erickson, and Mark Radwin for assisting us in the field. This work
722 developed through conversations and discussions with Ciarian Harmon, Tianqi Liu, Jason
723 Kelley, and two anonymous readers. We thank Dave Bowling and Heather Holmes for sharing
724 their equipment with us. This work was made possible with former BLM West Desert District
725 office staff's support, including Kevin Oliver, Matt Preston, Mike Nelson, Cheryl Johnson, Steve
726 Allen, and Roxanne Tea. Russ Draper support was essential for this project's success. An NSF
727 Coupled Natural Human Systems Award #1617473 to Brenda Bowen and a University of Utah
728 Global Change and Sustainability Center Graduate Student Research Grant funded this research.
729 The authors and their affiliations do not have any real or perceived financial conflicts in
730 performing this research.

731 **Data Availability Statement**

732 The data that support the findings of this study are openly available in Zenodo at
733 <https://doi.org/10.5281/zenodo.4171332>, <https://doi.org/10.5281/zenodo.4268710>, and
734 <https://doi.org/10.5281/zenodo.5634172>. The code that supports this work is archived at
735 <https://doi.org/10.5281/zenodo.5671739>.

736 **References**

- 737 Allen, R. G., Pereira, L. S., Raes, D., & Smith, M. (1998). *FAO Irrigation and Drainage Paper*
 738 *No. 56. Irrigation and Drainage* (Vol. 300). Rome, Italy.
 739 <https://doi.org/10.1016/j.eja.2010.12.001>
- 740 Allison, G. B., & Barnes, C. J. (1985). Estimation of evaporation from the normally “dry” Lake
 741 Frome in South Australia. *Journal of Hydrology*, 78(3–4), 229–242.
 742 [https://doi.org/10.1016/0022-1694\(85\)90103-9](https://doi.org/10.1016/0022-1694(85)90103-9)
- 743 Benison, K. C., & Bowen, B. B. (2006). Acid saline lake systems give clues about past
 744 environments and the search for life on Mars. *Icarus*, 183(1), 225–229.
 745 <https://doi.org/10.1016/j.icarus.2006.02.018>
- 746 Benison, K. C., & Karmanocky, F. J. (2014). Could microorganisms be preserved in Mars
 747 gypsum? Insights from terrestrial examples. *Geology*, 42(7), 615–617.
 748 <https://doi.org/10.1130/G35542.1>
- 749 Bernau, J., & Bowen, B. B. (2020). Time lapse imagery and field photos of the surface of the
 750 Bonneville Salt Flats. <https://doi.org/10.5281/zenodo.4171332>
- 751 Bernau, J., & Bowen, B. B. (2021). Depositional and early diagenetic characteristics of modern
 752 saline pan deposits at the Bonneville Salt Flats, Utah, USA. *Sedimentology*, sed.12861.
 753 <https://doi.org/10.1111/sed.12861>
- 754 Bethke, C. M. (2013). *Geochemical and Biogeochemical Reaction Modeling. Journal of*
 755 *Chemical Information and Modeling* (Vol. 53). Cambridge, UK: Cambridge University
 756 Press.
- 757 Boutt, D. F., Hynek, S. A., Munk, L. A., & Corenthal, L. G. (2016). Rapid recharge of fresh
 758 water to the halite-hosted brine aquifer of Salar de Atacama, Chile. *Hydrological Processes*,
 759 30(25), 4720–4740. <https://doi.org/10.1002/hyp.10994>
- 760 Bowen, B. B., Kipnis, E. L., & Raming, L. W. (2017). Temporal dynamics of flooding,
 761 evaporation, and desiccation cycles and observations of salt crust area change at the
 762 Bonneville Salt Flats, Utah. *Geomorphology*, 299, 1–11.
 763 <https://doi.org/10.1016/j.geomorph.2017.09.036>
- 764 Bowen, B. B., Kipnis, E. L., & Pechmann, J. M. (2018). Observations of salt crust thickness
 765 change at the Bonneville Salt Flats from 2003–2016. In S. H. Emerman, B. B. Bowen, S.
 766 Simmons, & S. Schamel (Eds.), *Geofluids of Utah* (47th ed., pp. 247–285). Utah Geological
 767 Association Publication.
- 768 Bowen, B. B., Bernau, J., Kipnis, E., Lerback, J., Wetterlin, L., & Kleba, B. (2018). The making
 769 of a perfect racetrack at the Bonneville Salt Flats. *The Sedimentary Record*, 16(2), 4–11.
- 770 de Bruin, H., & Holstag, A. (1982). A simple parameterization of surface fluxes of sensible and
 771 latent heat during daytime compared with the Penman–Monteith concept. *Journal of*
 772 *Applied Meteorology and Climatology*, 21(1), 1610–1621.
- 773 Calder, I. R., & Neal, C. (1984). Evaporation from saline lakes: A combination equation
 774 approach. *Hydrological Sciences Journal*, 29(1), 89–97.
 775 <https://doi.org/10.1080/02626668409490924>

- 776 Chapman, S., & Lindzen, R. S. (1970). Atmospheric tides : thermal and gravitational, 212.
- 777 Costelloe, J. F., Matic, V., Western, A. W., Walker, J. P., & Tyler, M. (2011). Field estimates of
778 groundwater discharge - Great Artesian Basin, South Australia. *MODSIM 2011 - 19th*
779 *International Congress on Modelling and Simulation*, (December), 2100–2106.
- 780 Craft, K. M., & Horel, J. D. (2019). Variations in surface albedo arising from flooding and
781 desiccation cycles on the Bonneville Salt Flats, Utah. *Journal of Applied Meteorology and*
782 *Climatology*, 58(4), 773–785. <https://doi.org/10.1175/JAMC-D-18-0219.1>
- 783 Crosbie, R. S., Binning, P., & Kalma, J. D. (2005). A time series approach to inferring
784 groundwater recharge using the water table fluctuation method. *Water Resources Research*,
785 41(1), 1–9. <https://doi.org/10.1029/2004WR003077>
- 786 Crosbie, R. S., Doble, R. C., Turnadge, C., & Taylor, A. R. (2019). Constraining the Magnitude
787 and Uncertainty of Specific Yield for Use in the Water Table Fluctuation Method of
788 Estimating Recharge. *Water Resources Research*, 55(8), 7343–7361.
789 <https://doi.org/10.1029/2019WR025285>
- 790 Van Dam, R. L., Simmons, C. T., Hyndman, D. W., & Wood, W. W. (2009). Natural free
791 convection in porous media: First field documentation in groundwater. *Geophysical*
792 *Research Letters*, 36(11), 1–5. <https://doi.org/10.1029/2008GL036906>
- 793 DeMeo, G. A., Laczniak, R. J., Boyd, R. A., Smith, J. L., & Nylund, W. E. (2003). *Estimated*
794 *ground-water discharge by evapotranspiration from Death Valley, California, 1997–2001*.
795 Carson City, NV.
- 796 Duffy, C. J., & Al-Hassan, S. (1988). Groundwater circulation in a closed desert basin:
797 Topographic scaling and climatic forcing. *Water Resources Research*, 24(10), 1675–1688.
798 <https://doi.org/10.1029/WR024i010p01675>
- 799 Duke, H. R. (1972). Capillary Properties of Soils - Influence Upon Specific Yield. *Transactions*
800 *of the ASAE*, 15(4), 0688–0691. <https://doi.org/10.13031/2013.37986>
- 801 Fan, Y., Duffy, C. J., & Oliver, D. S. (1997). Density-driven groundwater flow in closed desert
802 basin: Field investigations and numerical experiments. *Journal of Hydrology*, 196, 139–184.
803 [https://doi.org/10.1016/S0022-1694\(96\)03292-1](https://doi.org/10.1016/S0022-1694(96)03292-1)
- 804 Garcia, C. A., Huntington, J. M., Buto, S. G., Moreo, M. T., Smith, J. L., & Andraski, B. J.
805 (2015). Groundwater Discharge by Evapotranspiration, Dixie Valley, West-Central Nevada,
806 March 2009–September 2011. *U.S. Geological Survey Professional Paper*, (1805), 1–90.
807 <https://doi.org/http://dx.doi.org/10.3133/pp1805>
- 808 Gerla, P. J. (1992). The relationship of water-table changes to the capillary fringe,
809 evapotranspiration, and precipitation in intermittent wetlands. *Wetlands*, 12(2), 91–98.
810 <https://doi.org/10.1007/BF03160590>
- 811 Gillham, R. W. (1984). The capillary fringe and its effect on water-table response. *Journal of*
812 *Hydrology*, 67(1–4), 307–324. [https://doi.org/10.1016/0022-1694\(84\)90248-8](https://doi.org/10.1016/0022-1694(84)90248-8)
- 813 Gonthier, G. J. (2007). A Graphical Method for Estimation of Barometric Efficiency from
814 Continuous Data — Concepts and Application to a Site in the Piedmont , Scientific
815 Investigation Report 2007-5111 Prepared in cooperation with the U.S. Air Force
816 Aeronautical Systems Center, M. U. S. Geological Survey Scientific Investigation Report

- 817 2007-5111, 38.
- 818 Hang, C., Nadeau, D. F., Jensen, D. D., Hoch, S. W., & Pardyjak, E. R. (2016). Playa soil
819 moisture and evaporation dynamics during the MATERHORN field program. *Boundary-*
820 *Layer Meteorology*, 159(3), 521–538. <https://doi.org/10.1007/s10546-015-0058-0>
- 821 Healy, R. W., & Cook, P. G. (2002). Using groundwater levels to estimate recharge.
822 *Hydrogeology Journal*, 10(1), 91–109. <https://doi.org/10.1007/s10040-001-0178-0>
- 823 Heliotis, F. D., & DeWitt, C. B. (1987). Rapid Water Table Responses to Rainfall in a Northern
824 Peatland Ecosystem. *JAWRA Journal of the American Water Resources Association*, 23(6),
825 1011–1016. <https://doi.org/10.1111/j.1752-1688.1987.tb00850.x>
- 826 Horel, J., Splitt, M., Dunn, L., Pechmann, J., White, B., Ciliberti, C., et al. (2002). Mesowest:
827 Cooperative mesonets in the western United States. *Bulletin of the American*
828 *Meteorological Society*, 83(2), 211–225.
- 829 Huntington, J. M., Garcia, A., & Rosen, M. R. (2014). Hydrogeologic framework and
830 occurrence, movement, and chemical characterization of groundwater in Dixie Valley,
831 west-central Nevada. *U.S. Geological Survey Scientific Investigations Report, 2014–5152*,
832 60. <https://doi.org/http://dx.doi.org/10.3133/sir20145152>
- 833 Jackson, T. R., Halford, K. J., Gardner, P. M., & Garcia, A. (2018). Evaluating
834 micrometeorological estimates of groundwater discharge from Great Basin desert playas.
835 *Groundwater*, 56(6), 909–920. <https://doi.org/10.1111/gwat.12647>
- 836 Jacobson, G., & Jankowski, J. (1989). Groundwater-discharge processes at a central Australian
837 playa. *Journal of Hydrology*, 105(3–4), 275–295. [https://doi.org/10.1016/0022-](https://doi.org/10.1016/0022-1694(89)90109-1)
838 [1694\(89\)90109-1](https://doi.org/10.1016/0022-1694(89)90109-1)
- 839 Jensen, D. D., Nadeau, D. F., Hoch, S. W., & Pardyjak, E. R. (2016). Observations of near-
840 surface heat-flux and temperature profiles through the early evening transition over
841 contrasting surfaces. *Boundary-Layer Meteorology*, 159(3), 567–587.
842 <https://doi.org/10.1007/s10546-015-0067-z>
- 843 Kampf, S. K., & Tyler, S. W. (2006). Spatial characterization of land surface energy fluxes and
844 uncertainty estimation at the Salar de Atacama, Northern Chile. *Advances in Water*
845 *Resources*, 29(2), 336–354. <https://doi.org/10.1016/j.advwatres.2005.02.017>
- 846 Kampf, S. K., Tyler, S. W., Ortiz, C. A., Muñoz, J. F., & Adkins, P. L. (2005). Evaporation and
847 land surface energy budget at the Salar de Atacama, northern Chile. *Journal of Hydrology*,
848 310(1–4), 236–252. <https://doi.org/10.1016/j.jhydrol.2005.01.005>
- 849 Kang, M., Ichii, K., Kim, J., Indrawati, Y. M., Park, J., Moon, M., et al. (2019). New gap-filling
850 strategies for long-period flux data gaps using a data-driven approach. *Atmosphere*, 10(10),
851 1–18. <https://doi.org/10.3390/atmos10100568>
- 852 Kelley, J. (2020). Assessment and correction of solar radiation measurements with simple neural
853 networks. *Atmosphere*, 11(11). <https://doi.org/10.3390/atmos11111160>
- 854 Kelley, J., & Pardyjak, E. R. (2019). Using neural networks to estimate site-specific crop
855 evapotranspiration with low-cost sensors. *Agronomy*, 9(2).
856 <https://doi.org/10.3390/agronomy9020108>

- 857 Kelley, J., Mccauley, D., Alexander, G. A., Iv, W. F. G., Siegfried, R., & Oldroyd, H. J. (2020).
858 Using machine learning to integrate on-farm sensors and agro-meteorology networks into
859 site-specific decision support, *63*(5), 1427–1439.
- 860 Kipnis, E. L., & Bowen, B. B. (2018). Observations of salt crust change from 1960-2016 and the
861 role of humans as geologic agents at the Bonneville Salt Flats, Utah. In S. H. Emerman, B.
862 B. Bowen, S. Simmons, & S. Schamel (Eds.), *Geofluids of Utah* (47th ed., pp. 287–301).
863 Utah Geological Association Publication.
- 864 Kipnis, E. L., Bowen, B. B., Hutchings, S. J., Hynek, S. A., & Benison, K. C. (2020). Major ion
865 geochemistry in Na-Ca-Mg-K-Cl-SO₄ brines using portable X-ray fluorescence
866 spectrometry. *Chemical Geology*, 135577.
867 <https://doi.org/https://doi.org/10.1016/j.chemgeo.2020.119865>
- 868 Lerback, J. C., Hynek, S. A., Bowen, B. B., Bradbury, C. D., Solomon, D. K., & Fernandez, D.
869 P. (2019). Springwater provenance and flowpath evaluation in Blue Lake, Bonneville basin,
870 Utah. *Chemical Geology*, 529(April), 119280.
871 <https://doi.org/10.1016/j.chemgeo.2019.119280>
- 872 Li, X., & Shi, F. (2019). The effect of flooding on evaporation and the groundwater table for a
873 salt-crust soil. *Water (Switzerland)*, 11(5). <https://doi.org/10.3390/w11051003>
- 874 Lines, G. C. (1978). *Selected ground-water data, Bonneville Salt Flats and Pilot Valley, western*
875 *Utah. UGS.* https://doi.org/10.1007/978-94-017-4477-5_19
- 876 Lines, G. C. (1979). Hydrology and surface morphology of the Bonneville Salt Flats and Pilot
877 Valley playa, Utah. *Geological Survey Water-Supply Paper 2057*, (2057), 1–107.
- 878 Lowenstein, T. K., & Hardie, L. A. (1985). Criteria for the recognition of salt-pan evaporites.
879 *Sedimentology*, 32(5), 627–644. <https://doi.org/10.1111/j.1365-3091.1985.tb00478.x>
- 880 Lowenstein, T. K., Spencer, R. J., & Pengxi, Z. (1989). Origin of ancient potash evaporites:
881 Clues from the modern nonmarine Qaidam Basin of western China. *Science*, 245(4922),
882 1090–1092.
- 883 Lv, M., Xu, Z., Yang, Z. L., Lu, H., & Lv, M. (2021). A Comprehensive Review of Specific
884 Yield in Land Surface and Groundwater Studies. *Journal of Advances in Modeling Earth*
885 *Systems*, 13(2), 1–24. <https://doi.org/10.1029/2020MS002270>
- 886 Macumber, P. G. (1991). *Interaction between groundwater and surface systems in Northern*
887 *Victoria*. East Melbourne, Victoria, Australia: Department of Conservation and
888 Environment.
- 889 Malek, E., & Bingham, G. E. (1990). Evapotranspiration from the margin and moist playa of a
890 closed desert valley. *Journal of Hydrology*, 120, 15–34.
- 891 Marazuela, M. A., Vázquez-Suñé, E., Ayora, C., García-Gil, A., & Palma, T. (2019a).
892 Hydrodynamics of salt flat basins: The Salar de Atacama example. *Science of the Total*
893 *Environment*, 651, 668–683. <https://doi.org/10.1016/j.scitotenv.2018.09.190>
- 894 Marazuela, M. A., Vázquez-Suñé, E., Ayora, C., García-Gil, A., & Palma, T. (2019b). The effect
895 of brine pumping on the natural hydrodynamics of the Salar de Atacama: The damping
896 capacity of salt flats. *Science of the Total Environment*, 654, 1118–1131.
897 <https://doi.org/10.1016/j.scitotenv.2018.11.196>

- 898 Mardones, L. (1998). *Fluxes and evolution of saline solutions in the hydrological systems of*
899 *Ascotan and Atacama salars*. University of Paris.
- 900 Marticorena, B., Kardous, M., Bergametti, G., Callot, Y., Chazette, P., Khatteli, H., et al. (2006).
901 Surface and aerodynamic roughness in arid and semiarid areas and their relation to radar
902 backscatter coefficient. *Journal of Geophysical Research: Earth Surface*, 111(3).
903 <https://doi.org/10.1029/2006JF000462>
- 904 Mason, J. L., & Kipp, K. L. (1998). Hydrology of the Bonneville Salt Flats, northwestern Utah,
905 and simulation of ground-water flow and solute transport in the shallow-brine aquifer. *U.S.*
906 *Geological Survey Professional Paper 1585*, 108.
- 907 Mason, J. L., Brothers, W. C., Gerner, L. J., & Muir, P. S. (1995). *Selected hydrologic data for*
908 *the Bonneville Salt Flats and Pilot Valley, western Utah, 1991-93*. U.S. Geological Survey
909 *Open-File Report 95-104*. Salt Lake City, Utah.
- 910 MathWorks. (2020a). Deep Learning Toolbox. Natick, MA, USA: The Mathworks Inc.
- 911 MathWorks. (2020b). Matlab R2020b. Natick, MA, USA.
- 912 McMillan, T. C., Rau, G. C., Timms, W. A., & Andersen, M. S. (2019). Utilizing the Impact of
913 Earth and Atmospheric Tides on Groundwater Systems: A Review Reveals the Future
914 Potential. *Reviews of Geophysics*, 57(2), 281–315. <https://doi.org/10.1029/2018RG000630>
- 915 Menking, K. M., Anderson, R. Y., Brunsell, N. A., Allen, B. D., Ellwein, A. L., Loveland, T. A.,
916 & Hostetler, S. W. (2000). Evaporation from groundwater discharge playas, Estancia Basin,
917 central New Mexico. *Global and Planetary Change*, 25(1–2), 133–147.
918 [https://doi.org/10.1016/S0921-8181\(00\)00025-4](https://doi.org/10.1016/S0921-8181(00)00025-4)
- 919 Meyer, F. A. (1960). Effect of temperature on ground-water levels. *Journal of Geophysical*
920 *Research*, 65(6), 1747–1752. <https://doi.org/10.2118/65-04-09>
- 921 Mor, Z., Assouline, S., Tanny, J., Lensky, I. M., & Lensky, N. G. (2018). Effect of water surface
922 salinity on evaporation: The case of a diluted buoyant plume over the Dead Sea. *Water*
923 *Resources Research*, 54(3), 1460–1475. <https://doi.org/10.1002/2017WR021995>
- 924 Munk, L. A., Boutt, D. F., Moran, B. J., McKnight, S. V., & Jenckes, J. (2021). Hydrogeologic
925 and geochemical distinctions in freshwater-brine systems of an Andean salar. *Geochemistry,*
926 *Geophysics, Geosystems*. <https://doi.org/10.1029/2020gc009345>
- 927 Nachshon, U., Weisbrod, N., Dragila, M. I., & Grader, A. (2011). Combined evaporation and salt
928 precipitation in homogeneous and heterogeneous porous media. *Water Resources Research*,
929 47(3), 1–16. <https://doi.org/10.1029/2010WR009677>
- 930 Nachshon, U., Weisbrod, N., Katzir, R., & Nasser, A. (2018). NaCl crust architecture and its
931 impact on evaporation: Three-dimensional insights. *Geophysical Research Letters*, 45(12),
932 6100–6108. <https://doi.org/10.1029/2018GL078363>
- 933 Nield, J. M., King, J., Wiggs, G. F. S., Leyland, J., Bryant, R. G., Chiverrell, R. C., et al. (2013).
934 Estimating aerodynamic roughness over complex surface terrain. *Journal of Geophysical*
935 *Research Atmospheres*, 118(23), 12948–12961. <https://doi.org/10.1002/2013JD020632>
- 936 Nield, J. M., Bryant, R. G., Wiggs, G. F. S., King, J., Thomas, D. S. G., Eckardt, F. D., &
937 Washington, R. (2015). The dynamism of salt crust patterns on playas. *Geology*, 43(1), 31–

- 938 34. <https://doi.org/10.1130/G36175.1>
- 939 Post, V., Kooi, H., & Simmons, C. (2007). Using hydraulic head measurements in variable-
940 density ground water flow analyses. *Ground Water*, 45(6), 664–671.
941 <https://doi.org/10.1111/j.1745-6584.2007.00339.x>
- 942 Read, E. K., Carr, L., De Cicco, L., Dugan, H. A., Hanson, P. C., Hart, J. A., et al. (2017). Water
943 quality data for national-scale aquatic research: The Water Quality Portal. *Water Resources*
944 *Research*, 53(2), 1735–1745. <https://doi.org/10.1002/2016WR019993>
- 945 Robinson, E. S., & Bell, R. T. (1971). Tides in confined well- aquifer systems. *J Geophys Res*,
946 76(8), 1857–1869. <https://doi.org/10.1029/jb076i008p01857>
- 947 Rosen, M. R. (1994). The importance of groundwater in playas: A review of playa classifications
948 and the sedimentology and hydrology of playas. *Geological Society of America Special*
949 *Papers*, 289(January 1994), 1–18. <https://doi.org/10.1130/SPE289-p1>
- 950 Sanford, W. E., & Wood, W. W. (2001). Hydrology of the coastal sabkhas of Abu Dhabi, United
951 Arab Emirates. *Hydrogeology Journal*, 9(4), 358–366.
952 <https://doi.org/10.1007/s100400100137>
- 953 Schulz, S., Horovitz, M., Rausch, R., Michelsen, N., Mallast, U., Köhne, M., et al. (2015).
954 Groundwater evaporation from salt pans: Examples from the eastern Arabian Peninsula.
955 *Journal of Hydrology*, 531, 792–801. <https://doi.org/10.1016/j.jhydrol.2015.10.048>
- 956 Sieland, R. (2014). Hydraulic investigations of the Salar de Uyuni, Bolivia. *FOG - Freiberg*
957 *Online Geoscience*, 37(December 2014).
- 958 Stull, R. (2012). *An introduction to boundary layer meteorology* (Vol. 13). Springer Science &
959 Business Media. <https://doi.org/10.4267/2042/53468>
- 960 Turk, L. J. (1970). Evaporation of brine: A field study on the Bonneville Salt Flats, Utah. *Water*
961 *Resources Research*, 6(4), 1209–1215. <https://doi.org/10.1029/WR006i004p01209>
- 962 Turk, L. J. (1973). *Hydrogeology of the Bonneville Salt Flats*. Salt Lake City, UT: Utah
963 Geological and Mineral Survey.
- 964 Turk, L. J. (1975). Diurnal fluctuations of water tables induced by atmospheric pressure changes.
965 *Journal of Hydrology*, 26, 1–16.
- 966 Turk, L. J., Davis, S. N., & Bingham, C. P. P. (1973). Hydrogeology of lacustrine sediments,
967 Bonneville Salt Flats, Utah. *Economic Geology*, 68(1), 65–78.
968 <https://doi.org/10.2113/gsecongeo.68.1.65>
- 969 Turnadge, C., Crosbie, R. S., Barron, O., & Rau, G. C. (2019). Comparing Methods of
970 Barometric Efficiency Characterization for Specific Storage Estimation. *Groundwater*,
971 57(6), 844–859. <https://doi.org/10.1111/gwat.12923>
- 972 Tyler, S. W., Kranz, S., Parlange, M. B., Albertson, J., Katul, G. G., Cochran, G. F., et al. (1997).
973 Estimation of groundwater evaporation and salt flux from Owens Lake, California, USA.
974 *Journal of Hydrology*, 200(1–4), 110–135. [https://doi.org/10.1016/S0022-1694\(97\)00007-3](https://doi.org/10.1016/S0022-1694(97)00007-3)
- 975 Tyler, S. W., Muñoz, J. F., & Wood, W. W. (2006). The response of playa and sabkha hydraulics
976 and mineralogy to climate forcing. *Ground Water*, 44(3), 329–338.
977 <https://doi.org/10.1111/j.1745-6584.2005.00096.x>

- 978 Ullman, W. J. (1985). Evaporation rate from a salt pan: Estimates from chemical profiles in near-
979 surface groundwaters. *Journal of Hydrology*, 79(3–4), 365–373.
980 [https://doi.org/10.1016/0022-1694\(85\)90066-6](https://doi.org/10.1016/0022-1694(85)90066-6)
- 981 Walton, W. C. (1970). *Groundwater resource evaluation*. McGraw-Hill series in water resources
982 and environmental engineering. [https://doi.org/10.1016/0022-1694\(71\)90082-5](https://doi.org/10.1016/0022-1694(71)90082-5)
- 983 van Weert, F., & van der Gun, J. (2012). Saline and Brackish groundwater at shallow and
984 intermediate depths: Genesis and World Wide Occurrence. *2012 Congress of the Canadian*
985 *Branch of the International Association of Hydrogeologists (IAH)*, 1–9. Retrieved from
986 [https://www.un-igrac.org/es/resource/saline-and-brackish-groundwater-shallow-and-](https://www.un-igrac.org/es/resource/saline-and-brackish-groundwater-shallow-and-intermediate-depths-genesis-and-world-wide)
987 [intermediate-depths-genesis-and-world-wide](https://www.un-igrac.org/es/resource/saline-and-brackish-groundwater-shallow-and-intermediate-depths-genesis-and-world-wide)
- 988 Wooding, R. A., Tyler, S. W., White, I., & Anderson, P. A. (1997). Convection in groundwater
989 below an evaporating salt lake: 1. Onset of instability. *Water Resources Research*, 33(6),
990 1219–1228. <https://doi.org/10.1029/96WR03534>
- 991 Wurtsbaugh, W. A., Miller, C., Null, S. E., Justin De Rose, R., Wilcock, P., Hahnenberger, M.,
992 et al. (2017). Decline of the world’s saline lakes. *Nature Geoscience*, 10(11), 816–823.
993 <https://doi.org/10.1038/ngeo3052>